Pakistan Veterinary Journal

ISSN: 0253-8318 (PRINT), 2074-7764 (ONLINE)
DOI: 10.29261/pakvetj/2026.164

RESEARCH ARTICLE

Treatment and Mechanism of Total Flavonoids from Pueraria Flower on Nonalcoholic Steatohepatitis (NASH) Mice

Yan Luo[1,a], Yiheng Han[2,a], Ying Zhang[3,a], Baoying Chen[1,a], Qian Zhao[1], Wenying Bi[1], Jiatong Sui[1], Hongbing Duan[1], Fengcai Zou[1,4], Xiao Xiao[1,4,*] and Yi Wu[1,4,*]

[1]College of Veterinary Medicine, Yunnan Agricultural University, Kunming 650201, China; [2]Department of Geriatrics, Jiangsu Province Hospital of Chinese Medicine, Affiliated Hospital of Nanjing University of Chinese Medicine; [3]College of Veterinary Medicine, China Agricultural University, Beijing 100193, Beijing City, China; [4]The Yunnan Key Laboratory of Veterinary Etiological Biology, College of Veterinary Medicine, Yunnan Agricultural University, Kunming 650201, Yunnan Province, China. [a]These authors contributed equally to this article.
*Corresponding author: 961460716@qq.com; wuyi2001cn@163.com

ARTICLE HISTORY (26-657)

Received: June 07, 2026
Revised: July 21, 2026
Accepted: July 23, 2026
Published online: July 27, 2026

Key words:
Nonalcoholic Steatohepatitis
Total Flavonoids from
Pueraria Flower

ABSTRACT

Nonalcoholic steatohepatitis (NASH) is characterized by liver steatosis, inflammation and metabolic disorders, and current treatment options are limited. The total flavonoids extracted from the pueraria flower (TFP) have been reported to have antioxidant and hepatoprotective effects. However, the effects of TFP on NASH and its underlying mechanisms remain unclear. To gain more insight into the pharmaceutical value of TFP for treating NASH, the chemical composition of TFP was analyzed by UPLC–ESI–MS/MS. A NASH mouse model was established to evaluate the effects of TFP on liver and fat indices, serum biochemical parameters, and liver histopathology. The composition of the gut microbiota was analyzed by 16S rRNA sequencing, and the metabolome of the liver was studied. Thirty-five flavonoids were identified as the main components. In NASH mice, TFP was able to reduce liver and epididymal fat indices and decrease serum triglyceride, total cholesterol, low-density lipoprotein cholesterol, aspartate aminotransferase, and alanine aminotransferase levels. Histological analysis confirmed the reduction in lipid deposition and improvement in liver structure. Additionally, TFP helped restore microbial diversity, increase the abundance of beneficial bacteria, and correct the metabolic functions related to the gut microbiota. Metabolomic analysis indicated that TFP could reverse the bile acid, fatty acid, and amino acid metabolic disorders caused by NASH, reduce the levels of harmful metabolites, and restore the levels of beneficial metabolites. Collectively, our data reveal that TFP intervention correlates with comprehensive amelioration of NASH-associated pathological phenotypes, accompanied by restored intestinal microecology, corrected hepatic metabolic disorders, and balanced lipid signaling protein expression. While these multi-omic and biochemical observations establish correlative links between TFP treatment and improved liver function, definitive causal molecular cascades need further functional experimental verification along the gut-liver axis.

To Cite This Article: Luo Y, Han Y, Zhang Y, Chen B, Zhao Q, Bi W, Sui J, Duan H, Zou F, Xiao X and Wu Y, 2026. Treatment and mechanism of total flavonoids from pueraria flower on nonalcoholic steatohepatitis (NASH) mice. Pak Vet J, 46(7): 1708-1721. http://dx.doi.org/10.29261/pakvetj/2026.164

INTRODUCTION

NAFLD and its advanced pathological subtype NASH belong to progressive metabolic liver ailments that severely impair the growth and production performance of diverse farm animals (Han *et al*., 2023; Imtiaz *et al*., 2025). From the veterinary perspective, the pathological traits of NASH overlap substantially with poultry FLHS, whose core pathological manifestations cover insulin resistance, massive hepatic fat accumulation, inflammatory infiltration and progressive liver fibrosis (Tu *et al*., 2023; Zhao *et al*., 2025; Cao, 2026). High-performance laying hens and overfed waterfowl are susceptible to such lesions, which often trigger acute death and decreased egg output and cause massive economic losses in poultry breeding. Besides poultry, high-yield dairy cattle and captive

companion animals also suffer from fatty liver diseases, whose occurrence is closely linked to unbalanced nutrition, endocrine disorders and excessive oxidative damage (Qureshi *et al*., 2004; Hu *et al*., 2024).

Multiple pathological events including insulin resistance, intrahepatic lipid accumulation and persistent inflammation jointly facilitate NASH progression (Bashir *et al*., 2024), and hepatic fibrosis severity serves as a crucial predictive index of mortality for human and animal patients (Qureshi *et al*., 2004; Zhao *et al*., 2025; Qiu, 2026). FLHS is regarded as the terminal pathological phase of avian NAFLD, and sustained fat deposition can induce hepatocellular necrosis, hepatic hemorrhage or even liver rupture. For periparturient dairy cows, insufficient energy supply accelerates *in-vivo* fat decomposition, further causing triglyceride buildup in liver tissue and secondary ketosis to damage reproduction and lactation capacity.

Worldwide, NAFLD and its progressive NASH variant have become dominant chronic hepatic illnesses among humans and domestic animals, mainly resulting from high-calorie feeding, obesity and diabetes-induced metabolic dysfunction (Shu *et al*., 2024; Chen *et al*., 2025). Advanced NASH may evolve into hepatic cirrhosis or malignant hepatocellular carcinoma, shortening animal survival and reducing breeding productivity. Nutritional intervention helps prevent fatty liver, yet stable long-term feeding regulation is hard to realize under intensive breeding modes (Li *et al*., 2024). No dedicated veterinary medicines are available for animal NASH so far. Hence, developing low-toxic natural plant additives is essential to prevent NASH and FLHS, cut breeding losses and avoid subsequent metabolic and cardiovascular complications.

Pueraria Flower (PF) is the flower bud of *Pueraria lobata* (Willd.) Ohwi or *Pueraria thomsonii* Benth (Li *et al*., 2025). This herbal raw material has been applied as food and folk medicine across Asia for millennia. Traditional Chinese medicinal records describe PF as sweet and cool herb targeting stomach meridian, commonly used to relieve alcohol-caused liver damage, gastrointestinal hemorrhage and various digestive discomforts (Zhu *et al*., 2023). The biological activities of PF are closely related to its chemical constituents. Over the past decade, researchers have isolated and identified more than 180 of these components, which are classified into flavonoids, volatile oils, phenolic acids, triterpenoids, steroids, polysaccharides and others (Xiong *et al*., 2010). Accumulating modern pharmacology research has validated the diverse bioactivities of PF, including alleviating alcohol intoxication and protecting the liver, offering antioxidant and anti-inflammatory effects, demonstrating estrogenic activity, providing neuroprotection and showing antibacterial activity (Lertpatipanpong *et al*., 2020).

Flavonoids belong to natural plant polyphenols with extensive pharmacological properties including antioxidation, anti-inflammation, metabolic modulation and hepatic protection, and they also exert positive impacts on bone growth of animals (Celep *et al*., 2024; Vemula *et al*., 2024; Liu *et al*., 2025; Shaukat *et al*., 2025; Makatjane and Zhou, 2026). Many research data verify these compounds can effectively intervene the pathological progress of NAFLD, making them promising natural candidates for fatty liver prevention and therapy. Due to the growing global prevalence of NAFLD and shortage of effective therapeutic agents, more explorations focusing on flavonoid-mediated liver protection are urgently required.

Existing experimental results prove flavonoid extracts from diverse herbal plants delay NAFLD development via optimizing lipid metabolism, lowering oxidative injury and relieving intrahepatic fat accumulation. Different botanical flavonoids rely on disparate molecular pathways to improve fatty liver disorders: Citrus peel-derived flavonoids suppress NF-κB and MAPK cascades to achieve liver protection and anti-inflammatory outcomes in rat NAFLD models according to multi-omics findings (Jiang *et al*., 2019), It has been validated in preliminary high-throughput omics experiments that pure citrus-derived total flavonoids mitigate NAFLD by intervening in the TLR/CCL signaling pathway (Wu *et al*., 2017). Besides, flavonoid monomers separated from licorice via multi-step chromatographic purification and grapefruit-derived limonin obtained from enzymatic extraction both possess favorable anti-NAFLD bioactivity and adjust hepatic gluconeogenesis (Fang *et al*., 2025), Flavonoids extracted from Manchurian walnut bark are primarily applied against alcohol-induced fatty liver, and the molecular pathways validated via LC-MS/MS, network pharmacology and cellular experiments provide valuable references for developing anti-NASH flavonoid preparations (Bak *et al*., 2025). In addition, although the total flavonoids from Juglans mandshurica bark are used mainly to treat alcoholic fatty liver, their mechanism of action, as confirmed by LC–MS/MS, network pharmacology analysis and in vitro verification, also enlighten the research on the use of flavonoids for treating fatty liver-related diseases (Niu *et al*., 2024). Above research demonstrates flavonoids from different raw materials exert anti-fatty liver functions with distinct modes of action and promote the exploitation of natural anti-NAFLD medicines. Nevertheless, available literature rarely clarifies the exact efficacy and molecular regulatory routes of TFP against NASH. For this reason, the present study constructs MCD-induced NASH mouse models to explore TFP's in vivo curative effects and inner mechanisms, providing experimental evidence for the clinical utilization of TFP against NASH.

MATERIALS AND METHODS

Extraction of total flavonoids from *Flos puerariae*: Dry kudzu flower raw material was pre-soaked in distilled water over two hours ahead of extraction. Gradient hot reflux extraction was carried out stepwise with 90, 85 and 70% ethanol aqueous solutions separately. Every ethanol concentration was used for two repeated extractions lasting two hours each. All collected filtrates were combined, concentrated under vacuum environment before freeze-drying to gain crude TFP solid powder, then redissolved in distilled water to prepare 0.30 g/mL stock solution. The prepared liquid was loaded onto D101 macroporous adsorption resin; four column volumes of ultrapure water were adopted to wash away miscellaneous impurities, and

another four BV of 50% ethanol was applied to elute target flavonoids. Eluent was concentrated at identical temperature, and freeze-dried and final TFP powder was stored at 4℃ for subsequent experimental detection.

UPLC–ESI–MS–MS component analysis of TFP: Twenty milligrams of TFP powder was dissolved in 10mL methanol, ultrasonically treated for 10min under room temperature, then centrifuged at 12000rpm for another 10min. Supernatant was collected and filtered via 0.22μM microporous filter membrane prior to instrument injection. Chromatographic separation was completed on Halo-C18 analytical column at 30℃; flow speed was fixed at 0.3mL/min and injection volume set as 1μL. Mobile phase A was 0.05% formic acid aqueous solution and B was 0.05% formic acid acetonitrile solution with the same gradient elution schedule. ESI positive ionization mode was chosen for MS detection with unchanged source parameters and stepped collision energy settings for secondary mass scanning.

Experimental model and treatments: Six-week-old SPF-grade C57BL/6 mice (total n=72) were purchased from Kunming Medical University. One-week adaptive feeding was arranged under standardized breeding conditions before random grouping into six cohorts with twelve animals apiece. Based on existing pharmacological findings, silymarin was set as Silymarin medicine. Apart from blank control fed with regular feed, other five groups were supplied with MCD feed from Xietong Bioengineering over six weeks. All groups except for control received MCD diet for 6 weeks (Xietong Bioengineering Yanzhou Co., Ltd.). (1) Control group: standard normal diet (ND); (2) Model group: continued MCD diet; (3) Silymarin group: MCD+100 mg/kg; (4) TFPL: MCD+100 mg/kg TFP; (5) TFPM: MCD+200 mg/kg TFP; (6) TFPH: MCD+400 mg/kg TFP. Body weight of every mouse was recorded day by day throughout feeding cycle. After four weeks of continuous medication, all animals fasted for 24h before sacrifice, blood, caecum contents and hepatic specimens were gathered. Partial liver tissues were fixed with 4% paraformaldehyde for histological staining and surplus specimens stored at −80℃. All animal operations complied with ethics certification APYNAU 202503089.

Assessment of liver and epididymal fat indices: After euthanasia by cervical dislocation, the complete liver and epididymal fat pads were immediately dissected, tissues were mildly washed using precooled normal saline to wash away remaining blood stains, dried by filter paper blotting, followed by precise weighing.

Histological analysis of the liver: Following euthanasia, samples of the liver were promptly obtained, immersed in 4% formaldehyde solution for three days and then sliced into blocks measuring 3 millimeters in thickness. All tissue sections received a 20-minute washing process, followed by progressive dehydration in gradient ethanol, xylene clarification and paraffin embedding. Paraffin specimens were sliced and processed for HE staining: nuclear staining lasted 5min using hematoxylin, and cytoplasmic counterstaining was finished in 30s with eosin. After secondary dehydration and xylene treatment, neutral resin was used to mount slices. Histopathological features were visualized under SOPTOP ICX41 microscope, and relevant digital images were obtained by Image Viewer software. Nonalcoholic Steatohepatitis (NAS) scoring was conducted according to the standardized Kleiner scoring system: steatosis (0–3), lobular inflammation (0–3), hepatocellular ballooning (0–2); total NAS ranges from 0–8, with NAS ≥5 defined as definite NASH. All liver slice slides were coded and randomly reordered before blind evaluation by two independent pathologists without access to group information (single-blinded assessment). For hepatic fibrosis evaluation, Masson's trichrome staining was additionally performed on paraffin liver sections; collagen deposition area was quantified to assess early-stage fibrosis in MCD-fed mice, consistent with the fibrosis phenotype discussed in this work.

Oil red O staining: Once the tissue blocks were embedded in OCT compound, they were positioned onto the cryostat stage, with the temperature of the chamber being set appropriately. After optimizing the sectioning parameters, serial sections with a thickness of 8μL were cut and mounted onto slides pre-coated with poly-L-lysine. Tissue sections were kept at room temperature for natural air drying and 15 min fixation in 4% paraformaldehyde prior to staining, with surplus fixative washed off briefly by flowing water. Specimens were incubated for 8 min in freshly mixed Oil Red O working solution (0.5% Oil Red O: distilled water = 3:2) under subdued lighting conditions. Subsequently, the tissue sections underwent two rounds of differentiation using 60% isopropyl alcohol. Afterward, they were thoroughly rinsed with running water, followed by counterstaining with hematoxylin for a duration of 3 to 5 minutes. Following this, a brief differentiation step was performed in acid alcohol, which consists of 1% hydrochloric acid dissolved in 70% ethanol, lasting 2 seconds. The sections were then blued by immersion in running water for 3 minutes before being mounted using glycerol gelatin.

Periodic acid-Schiff-based histochemical detection: Paraffin sections were prepared following the procedure outlined in Section 2.5. Subsequently, these slices underwent oxidation by immersion in a 0.5–1% periodic acid solution for a duration of 5–10 minutes, followed by thorough rinsing with distilled water, and then exposure to Schiff's reagent for a period ranging from 15 to 30 minutes. Following these steps, the specimens were then counterstained by immersing them in hematoxylin, which resulted in the nuclei turning a distinct blue color after being thoroughly rinsed under running water until a rose-red hue was achieved. Serial treatments including differentiation, gradient ethanol dehydration, xylene transparency and neutral balsam mounting were conducted on processed specimens. Light microscopic observation on stained preparations was implemented to characterize the distribution of glycogen, polysaccharides and glycoproteins for biochemical component assessment.

Plasma marker measurement by ELISA: All acquired serum samples were refrigerated at 4℃. Double-antibody sandwich ELISA was adopted to test plasma biochemical

indexes. Triplicate 100μL aliquots from calibrators and diluted specimens were dispensed into prefabricated 96-well microplates. After 90 min incubation (37°C) and five-time buffer washing, 100μL HRP-coupled detecting antibody was supplemented for a 60-min incubation at 37°C. Additional washing steps were performed before adding 100μL TMB working solution, and chromogenic reaction proceeded at 37°C in darkness for 15min. Termination reagent was used to cease the reaction and instantaneous OD reading at 450nM was accomplished using full-spectrum microplate reader.

16S rRNA gene sequencing of feces: Fresh fecal samples were collected under sterile conditions and snap-frozen with liquid nitrogen, then shipped to Wuhan Bioyi Huineng Biotechnology Co., Ltd. For 16S rRNA high-throughput sequencing. Targeted amplification of the V3–V4 hypervariable segment within the 16S rRNA gene was completed using designated primer pairs. Purification and concentration determination were carried out for all amplified PCR fragments prior to sequencing library preparation. After library establishment, paired-end sequencing was performed on either Illumina MiSeq or Novaseq instrument. Raw sequencing reads were processed via standardized bioinformatic pipelines, including quality trimming, denoising, paired-read splicing and chimeric sequence removal to obtain qualified clean tags. Valid sequences were then clustered into OTUs or ASVs and assigned with taxonomic information for gut flora profiling. Microbial compositional features were finally interpreted based on alpha diversity, beta diversity, community constitution and differential species screening.

HPLC–MS/MS analysis: Untargeted metabolomic profiling was implemented via Vanquish UHPLC coupled to an Orbitrap Exploris 120 mass spectrometer (Thermo Fisher, Germany). Sample separation was achieved on a Hypersil Gold column (100 × 2.1mM, 1.9μM) adopting a 12 min linear gradient elution at 0.2mL/min flow velocity. Mobile phase formulation differed between ionization polarities: solvent A was 0.1% aqueous formic acid and solvent B was pure methanol under positive electrospray mode; conversely, 5mM ammonium acetate buffer (pH 9.0) and methanol served as mobile phases A and B for negative ion detection. Dual positive/negative MS acquisition was configured with 3.5 kV spray voltage, 320°C capillary temperature, 35 psi sheath gas pressure, 10L/min auxiliary gas, S-lens RF value set at 60, alongside 350°C auxiliary heater temperature.

Western blotting analysis: Total hepatic protein was extracted in RIPA lysis solution containing protease and phosphatase inhibitor cocktails. Protein concentration was determined via the BCA colorimetric assay. Equivalent protein loads were fractionated by SDS-PAGE before electrophoretic blotting onto PVDF membranes, followed by blocking treatment with TBST buffer. After sequential incubation with primary and corresponding secondary antibodies, target bands were visualized using ECL chemiluminescence reagent, and grayscale quantification was completed with ImageJ software. B-actin was utilized as internal reference for data normalization.

Data Statistics: Statistical analyses for numerical datasets were finished on GraphPad Prism 9.0; Shapiro–Wilk and Brown–Forsythe tests were separately applied to verify normality and homoscedasticity. One-way ANOVA coupled with Tukey's multiple comparison post-test was adopted for parametric datasets, and all measured values were expressed as mean±SEM, where $P<0.05$ represented statistically meaningful differences.

For microbiota sequencing, the V3–V4 hypervariable segments of 16S rRNA were sequenced on Illumina MiSeq. Raw reads were preprocessed with QIIME2 to obtain ASVs, which supported subsequent taxonomic classification, diversity evaluation, differential species screening as well as functional prediction via LEfSe, Random Forest and PICRUSt2 algorithms.

Table 1: Antibody Information

Antibody	Host	Dilution
ACC	Rabbit	1:500
CPT1A	Rabbit	1:1,000
PPARα	Rabbit	1:1,000
FASN	Rabbit	1:1,500
β-actin	Rabbit	1:2,500
Goat Anti-Rabbit IgG H&L (HRP)	Goat	1:8,000

In untargeted metabolomics, compound identification relied on KEGG, HMDB and LIPIDMaps databases. Multivariate algorithms including PCA and metaX-based PLS-DA together with univariate statistical assays were used to screen differential metabolites according to screening thresholds: VIP＞1, $P<0.05$, fold change ≥2 or ≤0.5. Volcano diagrams and heatmaps were plotted for data visualization, and Pearson correlation coefficient ® was calculated for correlation analysis. KEGG pathway enrichment was further conducted, with $P<0.05$ set as the cutoff for significant enrichment.

RESULTS

Composition of TFP: UPLC–ESI–MS/MS analysis of TFP revealed a total of 35 compounds (Table 2). The extract was primarily composed of isoflavone glycosides, including puerarin, daidzin, genistin, glycitin, and iridin. Xyloside derivatives such as 6″-β-D-xylosylgenistin and 6″-O-xylosyliridin were also detected. Isoflavone and flavonoid aglycones, including daidzein, genistein, apigenin, luteolin, quercetin, and kaempferol, were observed at longer retention times. The mass errors were within 5 ppm, and MS/MS fragmentation spectra revealed typical glycoside cleavage patterns (Fig. 1A & B). The present UPLC–ESI–MS/MS analysis only achieved qualitative identification of 35 flavonoid constituents in TFP, without external standard quantification of each compound's mass proportion. Therefore, we cannot accurately judge the exact contribution of each single flavonoid monomer to the hepatoprotective effect at this stage. Follow-up experiments will adopt standard reference substances to establish calibration curves, quantify the relative content of each isoflavone, and conduct independent intervention experiments of high-abundance monomers to clarify their individual therapeutic efficacy against NASH.

Table 2: Chemical constituents identified in TFP extract by UPLC–ESI–MS/MS

No	RT (min)	Molecular Formula	Theoretical mass(m/z)	Precursor mass (m/z)	Ion Mode	MS/MS (m/z)	Error (ppm)	Chemical Name
1	5.40	C22H22O10	446.40	445.1143	[M-H]-	445.1143, 325.0720, 325.0720	3.003	3′-Methoxy puerarin
2	3.82	C22H22O10	446.40	447.1277	[M+H]+	447.1277, 429.1174, 327.0857	-1.841	Glycitin
3	4.91	C26H28O14	564.49	563.1412	[M-H]-	563.1412, 383.0774, 353.0	2.909	6″-β-D-Xylosylgenistin
4	7.55	C27H30O15	594.52	593.1517	[M-H]-	593.1517, 299.0563, 284.0327	2.653	6″-O-Xylosyliridin
5	7.43	C22H22O10	446.40	447.1276	[M+H]+	447.1276, 285.0750, 270.0517	-2.266	Sissotrin
6	10.09	C21H20O10	432.40	431.0987	[M-H]-	431.0987, 298.0379, 240.0423	3.356	Genistin
7	8.38	C22H22O11	462.40	461.1093	[M-H]-	461.1093, 299.0562, 283.0250	3.258	Iridin
8	8.11	C27H30O15	594.50	593.1518	[M-H]-	593.1518, 434.4612, 299.0562	2.855	Kaempferol-3-O-rutinoside
9	14.05	C16H12O5	284.26	285.0752	[M+H]+	285.0752, 270.0517, 242.0569	-1.929	Biochanin A
10	10.09	C21H20O10	432.38	431.0987	[M-H]-	431.0987, 268.0379, 240.0423	3.356	Vitexin
11	18.14	C15H10O5	270.24	269.0457	[M-H]-	269.0457, 225.0552, 151.0442	4.572	Apigenin
12	12.80	C15H10O4	254.24	255.0647	[M+H]+	255.0647, 227.0700, 199, 0725,	-1.746	Daidzein
13	13.43	C16H12O5	284.26	285.0752	[M+H]+	285.0752, 270.0517, 253.0491,	-1.929	Glycitein
14	14.97	C15H10O6	286.24	285.0408	[M-H]-	285.0408, 268.0377, 240.0425,	4.931	Luteolin
15	19.72	C15H10O5	270.24	271.0595	[M+H]+	271.0595, 253.0491, 186.2213	-2.176	Genistein
16	18.49	C16H12O6	300.26	299.0563	[M-H]-	299.0563, 284.0328, 240.0426	4.198	Irisolidone
16	4.34	C23H24O11	476.40	477.1382	[M+H]+	477.1382, 459.1283, 357.0964	-1.882	Kakkalide
18	12.96	C15H10O4	254.24	253.0506	[M-H]-	253.0506, 217.8491, 180.9406	4.089	Daidzein
19	14.78	C15H10O6	286.24	287.0545	[M+H]+	153.0181, 169.0132, 231.0647	-3.598	Kaempferol
20	21.88	C16H12O4	268.26	267.0662	[M-H]-	61.9867, 96.9585, 223.0399	1.708	Formononetin
21	6.44	C21H20O9	416.38	415.1042	[M-H]-	112.9841, 139.0387, 253.0506	4.557	Puerarin
22	7.73	C21H22O11	450.40	449.10919	[M-H]-	151.0024, 178.9976, 285.0646	3.011	Dihydrokaempferol-3-O-glucoside
23	6.44	C21H20O9	416.38	415.1042	[M-H]-	112.9841, 139.0387, 225.0551	3.235	Daidzin
24	8.91	C27H30O15	594.52	593.1517	[M-H]-	227.0345, 255.0298, 285.0402	1.829	Irisolidone-7-O-xylosylglucoside
25	8.91	C27H30O15	594.52	593.1517	[M-H]-	121.0281, 227.0349, 283.0250	1.829	Kaempferol-3-O-rutinoside
26	14.63	C15H10O7	302.24	301.0356	[M-H]-	74.0231, 116.0492, 203.0820	2.699	Quercetin
27	16.94	C23H24O11	476.40	475.1251	[M-H]-	254.0218, 269.0457, 297.0407	2.218	Iristectorin
28	27.00	C17H14O5	298.29	299.0910	[M+H]+	84.9602, 158.9273, 186.2216	-3.171	3'-Oxymethy-daidzein-7 O-methylether
29	6.09	C26H28O14	564.49	563.1407	[M-H]-	117.0330, 269.0457, 297.0768	1.189	Genistein-O-pentosyl-hexoside
30	7.73	C21H22O11	450.40	449.1092	[M-H]-	449.1092, 303.0513, 285.0406	1.79	Dihydrokaempferol-O hexoside
31	6.89	C11H10O6	238.20	237.0400	[M-H]-	71.0122, 115.0023, 121.0281	6.89	Unknown
32	24.61	C16H12O5	284.26	283.0614	[M-H]-	173.0234, 227.0349, 268.0379	2.656	Kakkatin
33	9.88	C21H20O11	448.38	447.09354	[M-H]-	151.0024, 271.0613, 285.0408	1.798	6-Hydroxygenistein-7-O glucoside
34	7.38	C22H22O10	446.41	445.1149	[M-H]-	445.1149, 430.0902, 282.0536	4.441	Biochanin A-O-hexoside
35	1.76	C21H32O10	444.47	443.1925	[M-H]-	443.1925, 113.0228, 101.0229	2.925	Unknown

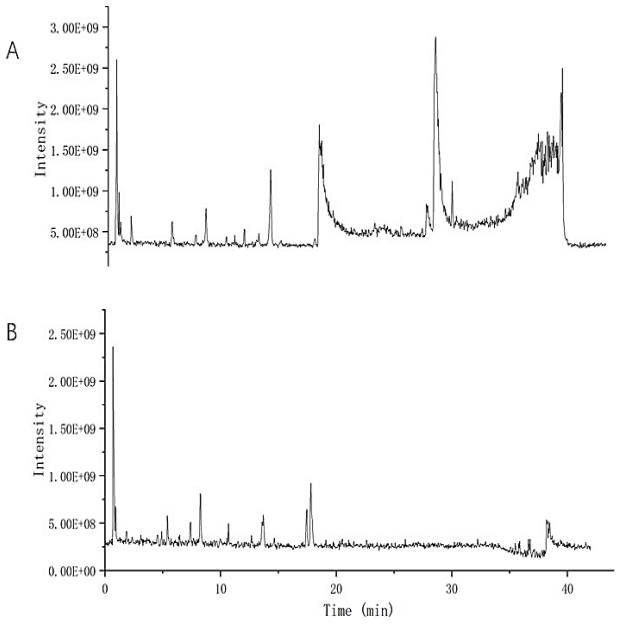

Fig. 1: Chemical composition of TFP. (A) Base peak chromatogram (BPC) of TFP in positive ion mode obtained by UPLC–ESI–MS/MS analysis. (B) Base peak chromatogram (BPC) of TFP in negative ion mode obtained by UPLC–ESI–MS/MS analysis.

Effects of TFP on body and liver parameters in NASH mice: In animal experiments, liver and epididymal fat coefficients were markedly elevated in the model cohort relative to blank controls ($P<0.01$). Nevertheless, intervention with TFP treatment was accompanied by dose-dependent attenuation of elevated liver and epididymal fat indices, concurrent with reduced intrahepatic lipid accumulation. (Fig. 2A and 2B).

Biochemical detection of peripheral blood revealed obvious upregulation in serum ALT and AST concentrations within model mice, indicative of severe hepatic injury. Meanwhile, the model group exhibited markedly higher concentrations of triglycerides (TG), total cholesterol (TC), and low-density lipoprotein cholesterol (LDL-C) compared to the control group, which signified the presence of lipid metabolism disruptions. In contrast, TFP administration effectively reversed these pathological changes, with the TFPH subgroup demonstrating the most pronounced improvements (Fig. 2C & D). Dose-dependent declines in these pathological serum markers were observed in TFP-treated mice, with the high-dose TFPH group showing the most prominent correlative improvement (Fig. 2E–G).

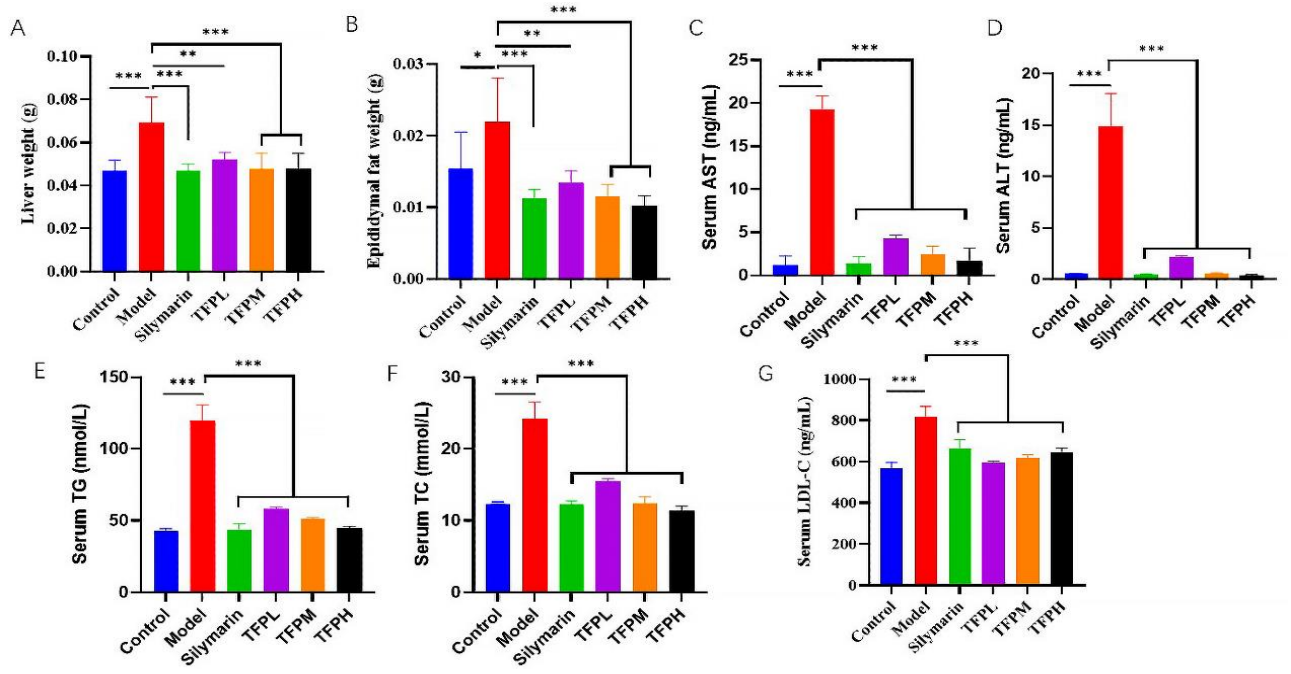

Fig. 2: Effects of TFP on liver parameters in NASH mice. (A) Liver weight index. (B) Epididymal fat index. (C) Serum AST levels. (D) Serum ALT levels. (E) Serum TG levels (F) Serum TC levels. (G) Serum LDL-C levels. The data are presented as the mean ± SD (n = 8 per group). **P<0.05, *P<0.01 vs. Model group.

In summary, the findings suggest that the TFP can enhance the health of the liver and fat tissues, reducing liver damage and improving lipid metabolism issues, with the highest dosage yielding the most pronounced positive effects.

Histopathological improvements in the liver in NASH mice: When examining tissue samples under a microscope, notable distinctions were observed across the various experimental groups. When examining the model group under a microscope, H&E staining demonstrated severely disrupted hepatic lobular arrangements, indistinct sinusoidal patterns, swollen liver cells, and significant fat accumulation. However, when treated with TFP, significant improvements were observed in the liver tissue: the hepatic lobular architecture returned to normal, the sinusoidal structures became clearer, and the lipid accumulation in hepatocytes was noticeably decreased in a dosage-dependent way, with the TFPH group demonstrating the most prominent protective effect (Fig. 3A). Oil Red O staining further confirmed these observations, revealing extensive lipid droplet accumulation in the Model group, while all treatment groups displayed significantly less lipid deposition. Notably, the degree of this improvement also displayed a dose-response relationship, with the highest TFPH dosage leading to the most significant reduction in lipid content (Fig. 3B). Quantitative analysis supported these results: compared with those in the Model group, the NASs in all treatment groups were significantly lower, with the strongest improvement observed in the TFPH group (P<0.01) (Fig. 3C). Similarly, the Oil Red O-positive area was significantly reduced following TFP administration, again most prominently in the TFPH group (P<0.01) (Fig. 3D). Collectively, these histological alterations were observed to correlate with TFP intervention in a dose-dependent mannerin mice afflicted with NASH, where the high-dose variant demonstrated the most remarkable safeguarding impacts.

TFP modulated the gut microbiota diversity induced by NASH: This part of the research focused on exploring the mechanisms by which TFPH intervention could restore the gut microbiota community structure in NASH mice. To assess the microbial community, the research utilized three indices: Shannon index, Simpson index, and Chao1 index, which are typically used to evaluate species diversity and abundance (see Fig. 4A–C for visualization). Statistical results indicated obvious decreases of these α-diversity indicators in NASH-modeled animals relative to healthy controls, illustrating that NASH pathogenesis triggered the loss of intestinal flora α-diversity. In contrast, TFPH supplementation produced favorable regulatory effects on gut microbial richness and diversity, restoring α-diversity close to the physiological level observed in blank control mice.

PCoA alongside NMDS were subsequently adopted to characterize global shifts in intestinal microbial composition induced by TFPH administration (Fig. 4D, E). According to PCoA outcomes, the top two principal axes collectively explained 70.88% of total community variation, with PCoA1 accounting for 51.6% and PCoA2 contributing 19.28% of the overall variance.

The PCoA score plot demonstrated a clear separation into three distinct clusters, suggesting that the gut microbiota composition of the model group underwent substantial modifications along the primary coordinate axis (PCoA1), exhibiting notable divergence from the control group (Con group). Conversely, PCoA-based microbial shifts in NASH mice were attenuated concurrent with TFPH treatment, with the treated group clustering closely to the control cohort. The trend of the NMDS results was similar to that of PCoA, with a stress value of 0.0172 (<0.05, indicating reliable analysis

results). The NMDS1 axis showed clear separation between the control group (Con group) and the model group, while the TFP group was positioned close to the control group, further demonstrating that this intervention had the ability to restore the overall structure of the microbiota. These findings suggested that NAFLD and the application of TFPH exerted notable impacts on the overall makeup of the gut microbiota, and TFPH was capable of effectively reversing the gut microbiota imbalance induced by NASH.

Regulatory effects of TFP on the gut microbiota: Species composition and differential analysis based on the sequencing results of the intestinal microbiota revealed significant hierarchical differences in the intestinal microbiota structure among the control group (Con), the model group (Model), and the TFP intervention group. At the phylum level, the intestinal microbiota of all three groups was dominated by the *Bacteroidota* and Firmicutes phyla, which were accompanied by low abundance distributions of phyla such as *Desulfobacterota* and

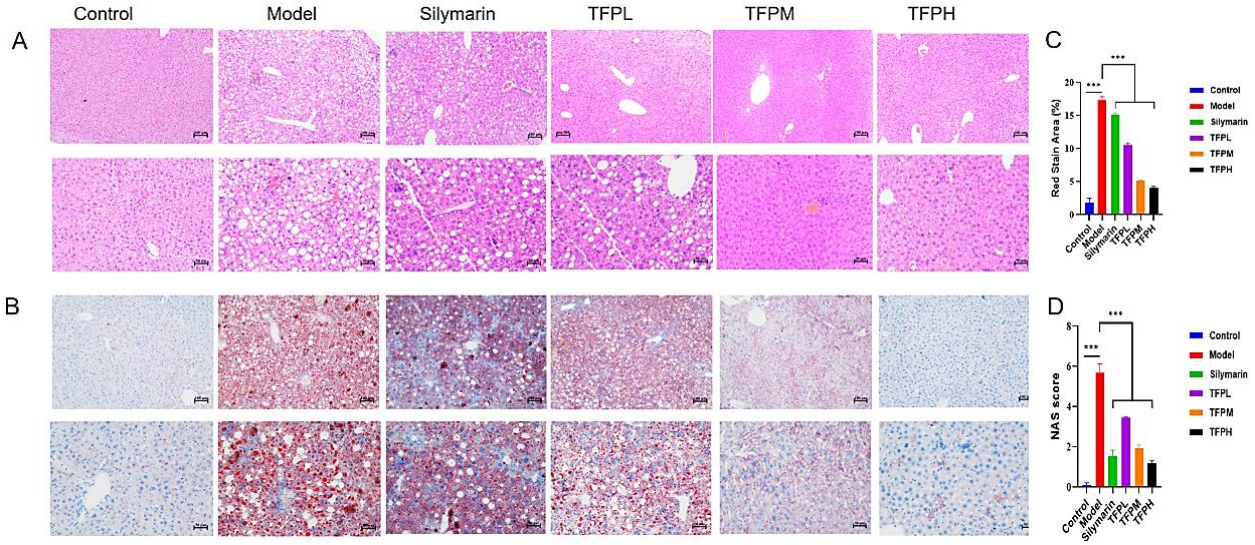

Fig. 3: Histological evaluation of liver tissues after TFP intervention in MCD-induced NASH mice. (A) H&E staining showing hepatic lobular architecture, hepatocyte ballooning and macrovesicular steatosis (scale bar=50μM). (B) Oil Red O staining visualizing intracellular neutral lipid droplets (scale bar=50μM). (C) Quantified total NASH Activity Score (NAS) calculated by standardized Kleiner scoring criteria (steatosis 0–3, lobular inflammation 0–3, hepatocellular ballooning 0–2); all tissue slides were randomly coded and blindly evaluated by two independent pathologists without group information. (D) Quantitative proportion of Oil Red O-positive lipid area in hepatic parenchyma. Parallel Masson's trichrome staining was performed on matched paraffin sections to quantify perisinusoidal collagen deposition for early hepatic fibrosis assessment. Data are expressed as mean ± SD (n = 8 per group). *P<0.05, **P<0.01 compared with Model group.

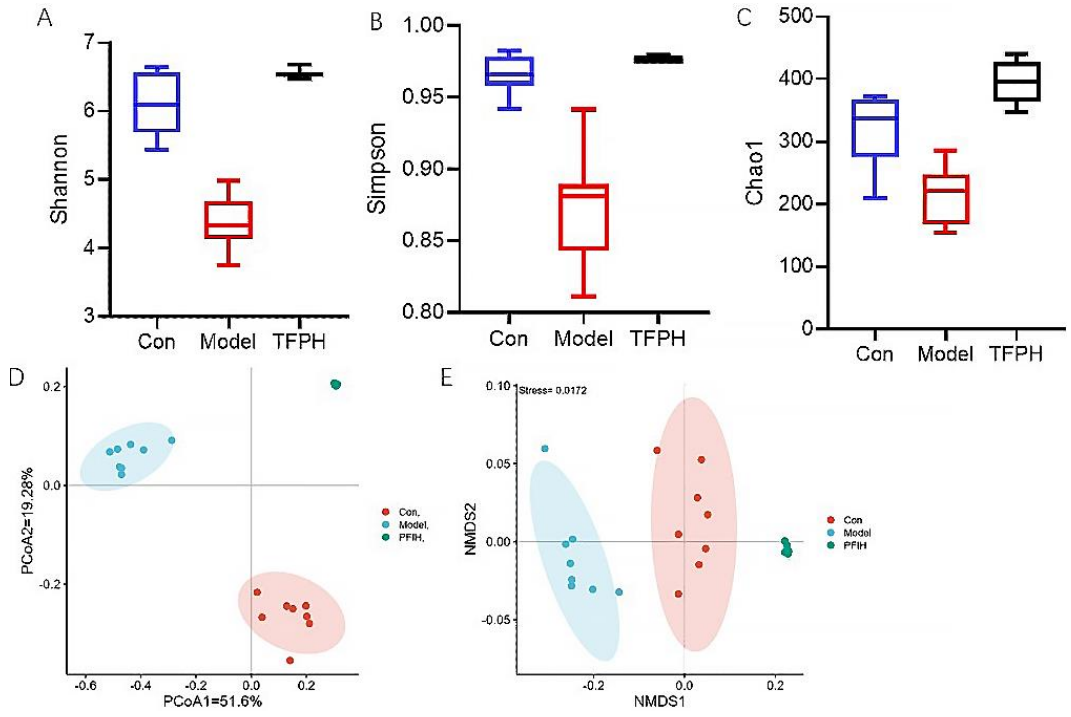

Fig. 4: (A) Structural modulation of the gut microbiota by the Chao index; (B) structural modulation of the gut microbiota by the Shannon index; (C) principal component analysis (PCA); (D) nonmetric multidimensional scaling (NMDS). Data are expressed as mean ± SD (n = 8 per group). *P<0.05, **P<0.01 compared with Model group.

Actinobacteria (Fig.5 A). Further focusing on the species composition at the genus and family levels, the dominant bacterial community structure in the model group was significantly reshaped compared with that in the control group, and after TFP intervention, the bacterial community composition spectrum visually tended to return to the level of the control group (Fig.5 B; Fig. 5C).

Quantitative analysis of the key advantage gates revealed that, compared with that in the control group, the relative abundance of the Firmicutes phylum in the model group significantly increased (Fig. 5 D), while the relative abundance of the *Bacteroidota* phylum significantly decreased (Fig. 5 E). Such reciprocal changes led to abnormal fluctuations in the ratio of the Firmicutes phylum to the Bacteroidota phylum (F/B) (Fig. 5 F). With respect to other key functional phyla, the relative abundance of the *Desulfobacterota* in the model group was significantly lower than that in the control group (Fig. 5G), while the relative abundance of the Actinobacteria phylum also tended to significantly increase (Fig. 5H). Beyond phylum-level compositional alterations, genus-level differential bacterial taxa were screened using the LEfSe algorithm. The MCD model group exhibited significant overgrowth of pro-inflammatory genus *Desulfovibrio*, while beneficial genera including *Bifidobacterium*, *Lactobacillus* and *Akkermansia* were markedly depleted after dietary modeling. TFPH intervention correlated with restored abundance of these protective taxa and suppressed proliferation of inflammatory bacteria (Fig. 5I). PICRUSt2 functional prediction further illustrated that MCD feeding disrupted intestinal pathways related to bile acid biosynthesis, short-chain fatty acid production and lipid digestion; TFP supplementation was accompanied by recovery of these impaired microbial metabolic functions. Detailed genus-level abundance heatmaps and LEfSe taxonomic cladograms are provided in Supplementary for in-depth (Fig. 5J) taxonomic analysis.: the abundance of the Firmicutes phylum decreased, while the abnormally low abundances of the Bacteroidota phylum and the *Desulfobacterota* significantly increased, and the abundance of the Actinobacteriota phylum significantly decreased.

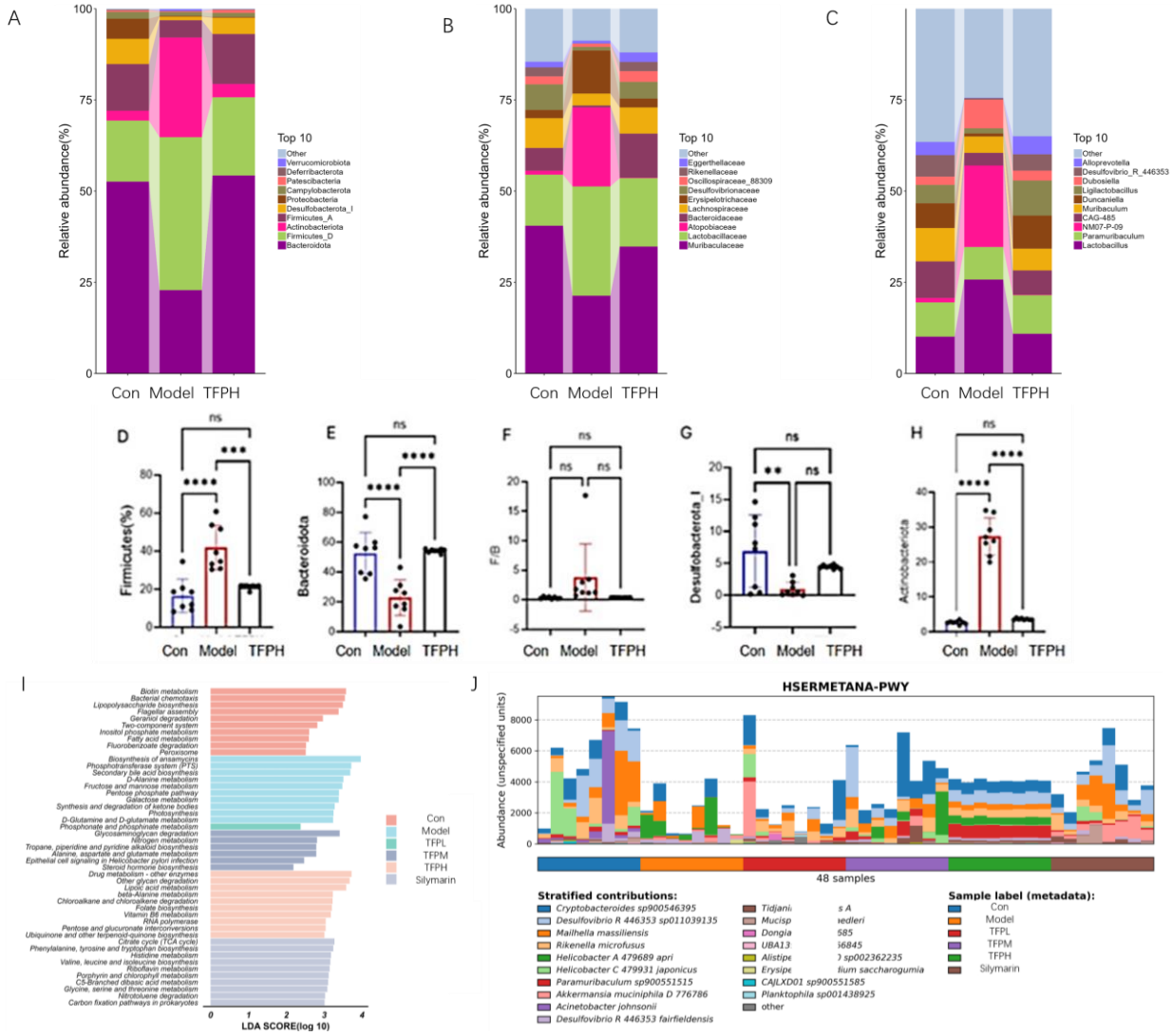

Fig. 5: Effects of TFPH on the gut microbiota composition in a mouse model. (A–C) Stacked bar charts showing the relative abundance of the top 10 bacterial taxa at the phylum (A), family (B), and genus (C) levels in the control (Con), model, and TFPH treatment groups(D–H) Quantitative analysis of the relative abundance of key bacterial taxa: (D) Firmicutes, € Bacteroidota, (F) the ratio of Firmicutes to Bacteroidota (F/B), (G) Desulfobacterota, and (H) Actinobacteria, (I) LEfSe analysis presented the LDA scores of taxa with significant differences in abundance. (J) Functional predictions through PICRUSt2 highlighted differences in amino acid, lipid, and energy metabolism pathways Data are expressed as mean ± SD (n = 8 per group). *P<0.05, **P<0.01 compared with Model group.

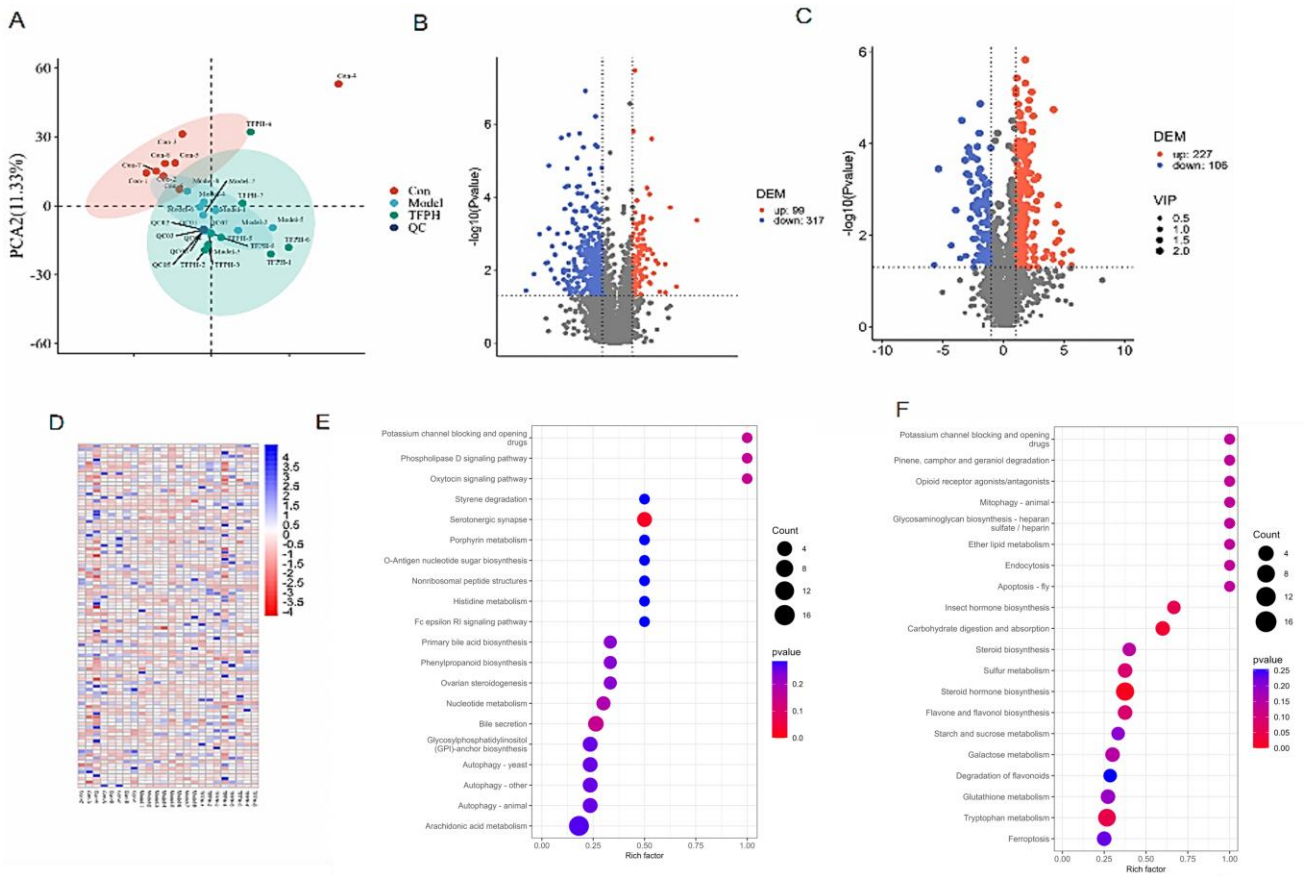

Fig. 6: Metabolomics analysis. (A) PCA plot of differentially abundant metabolites. (B, C) Volcano plot representing differentially abundant metabolites: the x-axis represents the fold change, and the y-axis represents significance. Red dots represent upregulated metabolites, green dots represent downregulated metabolites, and gray dots represent nonsignificant metabolites. (D) Metabolite level heatmap: the x-axis represents samples and clusters; the y-axis represents metabolites, with clusters (red = high expression, green = low expression). KEGG analysis of differentially abundant metabolites (E, F). Data are expressed as mean ± SD (n = 8 per group). *P<0.05, **P<0.01 compared with Model group.

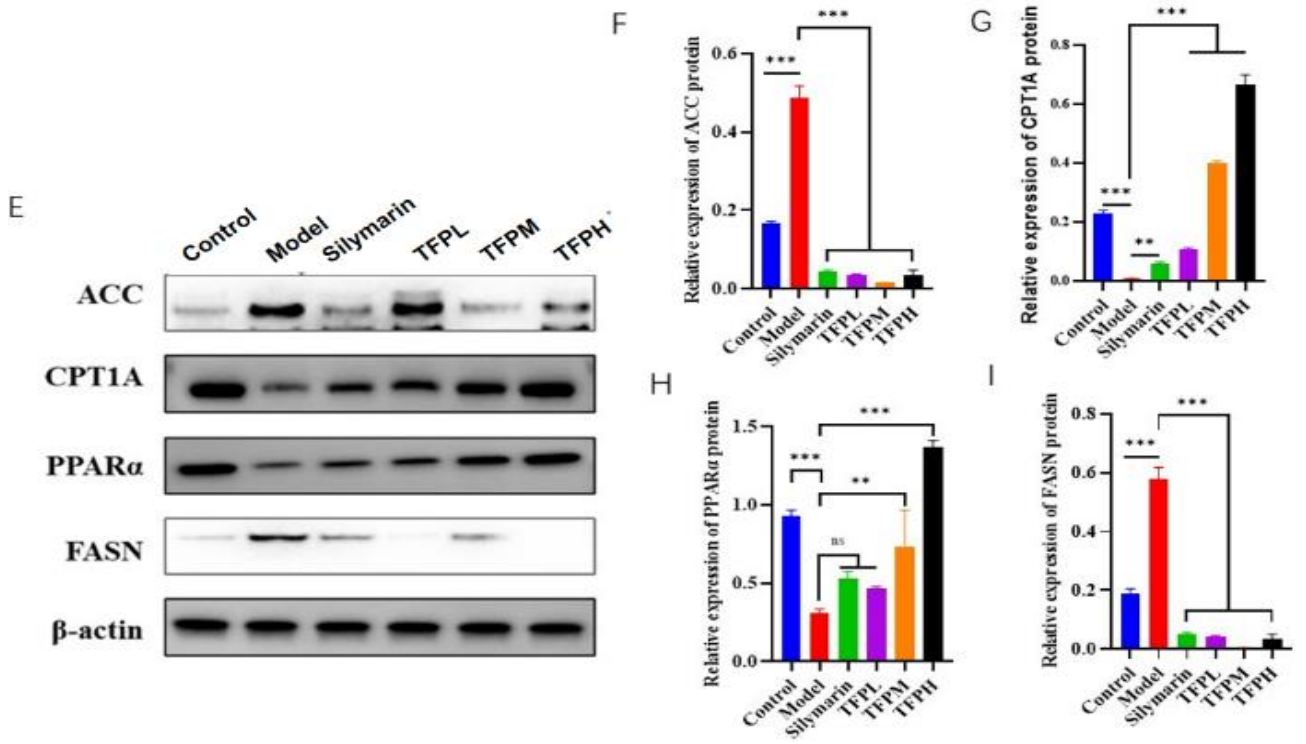

Fig. 7: Validation of lipid metabolism-related proteins. (A) Protein banding diagram. (B) ACC expression level. (C) CPT1A expression level. (D) PPARα expression level. (E) FASN expression level. Data are expressed as mean ± SD (n=8 per group). *P<0.05, **P<0.01 compared with Model group.

Effects of TFP on profiles of metabolites in colon contents: Principal component analysis (PCA) showed obvious spatial separation between the control and model groups along the PCA1 and PCA2 axes, demonstrating that the modeling procedure effectively induced profound alterations in endogenous metabolic profiles. Notably, the sample distribution of the TFPH treatment group (green) tended to cluster toward the control group, which illustrated that TFPH intervention could substantially rescue the metabolic disturbance triggered by modeling (Fig. 6A). A total of 416 differential metabolites were screened between the normal and model groups, among which 99 metabolites were significantly upregulated and 317 were downregulated (Fig. 6B). Meanwhile, comparison between the TFPH and model groups yielded 333 distinct metabolites, consisting of 227 upregulated and 106 downregulated molecules. These findings indicated that Normalized metabolite profiles were detected in TFPH-treated mice relative to untreated NASH controls in the model group. Unsupervised clustering analysis based on differential metabolite expression patterns achieved clear classification of the control, model and TFPH groups. Evident metabolic phenotypic differences were observed between the control and model groups, whereas the metabolic profile of the TFPH-treated group exhibited high similarity to the normal control group, which intuitively verified the ameliorative effect of TFPH on metabolic disorders.

The different metabolites in the normal control group and the model group were enriched mainly in pathways such as oxidative phosphorylation, sphingolipid metabolism, cysteine and methionine metabolism, suggesting that these pathways were significantly altered during model construction. The different metabolites in the TFP treatment group were enriched mainly in glycosphingolipid metabolism, cholesterol metabolism, glycerolipid metabolism, fat digestion/absorption, and insulin resistance metabolic pathways (Fig. 6E-F). To further verify the predicted lipid metabolism regulatory trend by metabolomics, key protein biomarkers related to lipid metabolism, such as PPARα, CPT1A, ACC, and FASN, were quantified by protein blotting. Protein blotting analysis (Fig. 7A) and quantitative statistics (Fig. 7B-E) indicated that Dose-dependent correlative changes in hepatic lipid regulatory proteins were observed following TFP intervention. Compared with that in the control group, the ACC protein expression in the model group was significantly greater. After TFP treatment, the expression of ACC significantly decreased, with the inhibitory effect being most prominent in the TFPH group (Fig. 7 B). The expression of CPT1A in the Model group was significantly lower than that in the Control group. After drug treatment, the expression of CPT1A significantly increased, whereas the TFPH group displayed the strongest upregulation effect (Fig. 7C). The expression of PPARα in the Model group was significantly lower than that in the Control group. Silymarin, TFPL, TFPM, and TFPH treatment significantly upregulated PPARα expression, among which the TFPH group presented the highest expression level (Fig. 7D). The expression of FASN in the Model group was originally much higher than that in the Control group. After TFPL, TFPM, and TFPH treatment, the FASN level significantly decreased, approaching the level of the control group (Fig.7 E). In summary, compared with the control group, the model group exhibited characteristics of lipid metabolism disorder, with increased expression of anabolic proteins (ACC and FASN) and decreased expression of catabolic proteins (CPT1A and PPARα). TFP treatment effectively reversed this trend, among which TFPH had the most significant regulatory effect on the above key proteins, suggesting its potential advantage in improving lipid metabolism disorder.

DISCUSSION

Nonalcoholic steatohepatitis (NASH) is a chronic progressive metabolic liver disorder that is prevalent in livestock and poultry and is characterized by excessive hepatic lipid deposition, hepatocellular injury and a hepatic inflammatory response (Xu *et al*., 2025; Cheng *et al*., 2025). Without effective intervention, the lesion gradually develops hepatic fibrosis, liver cirrhosis and even severe irreversible liver damage (Choi *et al*., 2022). Accurate animal NASH models should recapitulate typical pathological manifestations of spontaneous fatty liver disease in animals, including body fat accumulation, insulin resistance, dyslipidemia, obvious hepatic steatosis and progressive liver fibrosis (Abdolla, 2025). To date, no single experimental model can fully simulate all the pathogenic characteristics of spontaneous fatty liver syndrome in domestic animals (Li *et al*., 2023).

Methionine-choline deficient (MCD) diet induction serves as a classic and stable modeling approach for establishing animal NASH models. This modeling method can faithfully reproduce typical histopathological lesions of animal fatty liver injury, including hepatic lipid accumulation, lobular inflammation, hepatocellular ballooning degeneration and early hepatic fibrosis (Shu *et al*., 2024). However, the MCD model has prominent intrinsic drawbacks restricting its clinical translatability. Clinically, obesity and insulin resistance are central pathogenic drivers of human NASH, yet MCD feeding cannot induce these two key metabolic phenotypes; instead, MCD-treated mice tend to lose body weight without obvious insulin resistance. Given this gap between the model and human disease, the liver-protective effects observed in the current work cannot fully represent the drug efficacy in patients with metabolic dysfunction-associated NASH. Future studies will utilize HFD or combined dietary models with obesity and insulin resistance to complement and validate our present findings. In addition, livestock fatty liver hemorrhagic syndrome (FLHS) is triggered by overnutrition and obesity, while MCD-induced hepatic injury relies on choline/methionine-mediated lipid breakdown. This discrepancy limits direct extrapolation of our results to farm animal fatty liver disorders. All phenotypic and mechanistic conclusions drawn herein are specific to MCD-induced simple hepatic steatosis, rather than obesity-driven clinical NASH. Serum aspartate transaminase (AST) and alanine transaminase (ALT) are sensitive biochemical markers reflecting the degree of hepatocellular damage in diseased animals. In the present study, intervention withTFP markedly decreased serum AST and ALT concentrations in NASH model mice. HE staining and Oil Red O staining verified that the flavonoid extract effectively alleviated intrahepatic lipid droplet

deposition, relieved hepatic steatosis, suppressed hepatic inflammatory infiltration and retarded the progression of liver fibrosis. These findings demonstrated that Lonicera flavescens flavonoids strongly protect against animal NASH-related liver injury. Nevertheless, the exact molecular regulatory mechanism underlying its protective effect still needs further exploration.

The "gut–liver axis" is a channel for bidirectional material exchange between the liver and the intestine. Changes in the diversity and abundance of the intestinal microbiota not only affect choline metabolism, bile acid metabolism, and energy homeostasis and promote insulin resistance and inflammatory responses but also promote the production of harmful metabolites such as endotoxins and endogenous ethanol (Yan *et al*., 2025). These harmful metabolites can flow into the liver through the venous circulation and further accelerate the development of NASH (Zhan *et al*., 2024). It is speculated that total flavonoids from Pueraria flowers correlate with improved NASH phenotypes alongside remodeled intestinal microbiota. Therefore, in this study, 16S rRNA high-throughput sequencing technology was used to investigate the effects of total flavonoids from pueraria flower on the structure and composition of the intestinal microbiota in NASH mice. Alpha diversity refers to the diversity of microbiota in a specific area or ecosystem and is reflected by the index of the richness and evenness of the microbiota (Xiong *et al*., 2026). In our study, the Shannon index, Simpson index and Chao1 index of the intestinal microbiota in NASH mice significantly decreased, suggesting that the diversity of the intestinal microbiota in NASH mice decreased and that the dynamic balance of the intestinal microecology was disrupted. After the administration ofTFP, the diversity and richness of the intestinal microbiota in NASH mice significantly improved. Beta diversity reflects the similarity and difference of the microbiota structure among different samples, and the community composition structure is analyzed through PcoA, where greater distance between samples indicates greater difference. The results of this study's beta diversity analysis revealed that the structure of the intestinal microbiota in NASH mice significantly changed, and TFP treatment significantly improved the disorder of the intestinal microbiota structure in NASH mice and gradually restored it to a normal state.

Changes in the composition of the intestinal microbiota may also contribute to the occurrence of NASH (Du *et al*., 2025). In NASH patients, the relative abundance of potentially beneficial bacteria is low and is associated with the relative overgrowth of potentially harmful bacteria and a decrease in the diversity of the microbiota (Panyod *et al*., 2024). Therefore, an increase in the abundance of the Firmicutes phylum and a decrease in the abundance of the Bacteroidota phylum can be used as biomarkers to evaluate the progression of NASH (Hildebrandt *et al*., 2009).

This experiment revealed distinct intestinal microbial profiles among untreated control mice, untreated NASH model mice and TFP-treated mice. At the phylum level, compared with those in the control group, the abundance of bacteria in the Firmicutes phylum increased and the proportion of the Bacteroidota phylum decreased in the NASH group. Studies have shown that the intestinal microbiota of NASH mice has a relatively high Fimlicutes/ Bacteroidota (F/B, Firmicutes/ Bacteroidota) ratio, and this ratio has been used as an important indicator for determining the status of the human intestinal microbiota (Hildebrandt *et al*., 2009). Therefore, the elevated F/B ratio detected in NASH mice highlights the critical impact of dietary intervention on intestinal microbiota composition. (Zhu *et al*., 2015). The results of this study confirm that TFP has a regulatory effect on the intestinal microbiota composition in NASH model mice; it reverses the abnormal elevation of Firmicutes and depletion of Bacteroidota in NASH mice, thereby lowering the F/B ratio. Such interference may be due to the regulatory effect on the intestinal microbiota, in which the production of intestinal endotoxin is reduced, thereby improving NASH.

The Desulfobacterotais a sulfate-reducing bacterium that can reduce sulfate to hydrogen sulfide (H_2S). An appropriate amount of H_2S can maintain the function of the intestinal epithelial barrier and inhibit inflammation; however, excessive H_2S can damage the intestinal mucosa (Zhang *et al*., 2010). In this study, the abundance of the relative abundance of genus *Desulfovibrio* (phylum Desulfobacterota) was reduced, a change correlating with intestinal redox imbalance induced by MCD feeding. It weakened the protective effect of the intestinal barrier and thereby promoted intestinal endotoxinemia and aggravated liver inflammation and fibrosis. The phylum Actinobacteria (such as Bifidobacterium and Collinsella) plays a dual role in NAFLD/NASH. Beneficial bacteria (such as Bifidobacterium) can exert protective effects by regulating immunity and improving metabolism, whereas some opportunistic pathogens (such as *Collinsella aerofaciens*) are related to inflammation and metabolic disorders. In this study, the abundance of the phylum Actinobacteria increased, which may be a manifestation of the expansion of inflammatory-related bacteria in the microbiota disorder induced by the MCD diet or a compensatory response of the host to intestinal damage. Treatment with TFP significantly improved the intestinal microbiota structure in mice with NASH and gradually restored it to normal state.

This study systematically investigated the regulatory effect of TFPH on metabolic disorders in model animals and the potential underlying molecular mechanisms using nontargeted metabolomics combined with Western blotting technology. From the global characteristics of the metabolome to the level of key protein regulation, this study provides multidimensional experimental evidence that TFPH can help improve lipid metabolism disorders. The principal component analysis (PCA) results revealed that the sample points of the control group and the model group were significantly separated in terms of the PCA1 and PCA2 dimensions, indicating that the establishment of the model successfully induced specific changes in the metabolic profile. The sample points of the TFPH treatment group were significantly closer to those of the control group, and the metabolite difference analysis revealed that a total of 416 significantly different metabolites were identified between the control group and the model group, among which the number of downregulated metabolites was much greater than that of upregulated metabolites, suggesting that the model construction might mainly cause metabolic disorders by inhibiting the normal expression of multiple metabolites, while after TFPH intervention, the

differences in metabolites between the TFPH intervention group and the model group revealed that the upregulated metabolites accounted for a significantly greater proportion and that the downregulated metabolites were significantly reduced, indicating that the core regulatory effect of TFPH was to reverse the expression of metabolites that were inhibited in the model and to moderately inhibit the abnormally upregulated metabolites, thereby reconstructing the metabolic homeostasis of the organism. This feature is consistent with the typical pattern of natural active components that regulate metabolic disorders, namely, through the bidirectional regulation of abnormal metabolite expression to restore the metabolic balance of the organism (Su *et al*., 2022).

KEGG pathway enrichment analysis further revealed the core pathways targeted by TFPH in the regulation of metabolic disorders: the differentially abundant metabolites in the model group were enriched mainly in pathways such as oxidative phosphorylation, sphingolipid metabolism, and cysteine and methionine metabolism, indicating that energy metabolism, lipid signaling molecule metabolism, and amino acid metabolism were significantly disrupted when the disease model was established. Among them, abnormal sphingolipid metabolism has been confirmed to be closely related to liver lipid accumulation and metabolic imbalance, and abnormal sphingolipid metabolism can exacerbate lipid metabolic disorders and inflammatory responses (Eisinger *et al*., 2014); abnormal oxidative phosphorylation can cause energy metabolism disorders, further aggravating lipid metabolism disorders. After TFPH intervention, the differentially abundant metabolites were enriched mainly in glycosphingolipid metabolism, cholesterol metabolism, glycerolipid metabolism, fat digestion/absorption, and insulin resistance-related pathways, suggesting that the benefits of TFPH on metabolic disorders are highly focused on lipid metabolism and glycolipid metabolism interaction regulation pathways. As an important subgroup of sphingolipids, glycosphingolipid metabolism and metabolic abnormalities are closely related to various metabolic diseases, and targeting the regulation of glycosphingolipid metabolism has become a potential strategy for improving lipid disorders (Lombardo *et al*., 2012); moreover, abnormal cholesterol metabolism and glycerolipid metabolism are the leading causes of liver lipid accumulation, and insulin resistance and lipid metabolism disorders have a bidirectional regulatory relationship. The regulation of these pathways by TFPH further confirms that TFPH can improve the metabolic imbalance of organisms through synergistic effects among multiple pathways (Wei *et al*., 2024).

To verify the lipid metabolic regulatory trend predicted by metabolomics, a Western blot analysis of key proteins for liver lipid metabolism, namely, PPARα, CPT1A, ACC, and FASN, was performed. These results were in good agreement with the metabolomics results, further clarifying the molecular mechanism through which TFPH is accompanied by correlative changes in lipid metabolism. PPARα, as the core regulatory factor of liver lipid metabolism, mainly activates the expression of genes related to fatty acid β-oxidation, promoting fatty acid metabolism. The downregulation of PPARα directly leads to fatty acid oxidation disorder and the induction of lipid accumulation (Yan *et al*., 2023). The inhibition of CPT1A, the key rate-limiting enzyme of fatty acid β-oxidation, inhibits the entry of fatty acids into mitochondria for oxidative degradation, exacerbating lipid accumulation (Chen *et al*., 2024); ACC and FASN are the key enzymes involved in fatty acid synthesis metabolism. Their upregulation significantly promotes fatty acid synthesis and further aggravates lipid metabolism disorders. In this study, the significant downregulation of PPARα and CPT1A expression and significant upregulation of ACC and FASN expression in the model group indicate lipid metabolism disorder, which is consistent with the lipid metabolism protein expression patterns of abnormal metabolic models reported in previous studies.

TFP treatment reversed the abnormal expression of these proteins in a dose-dependent manner. Among them, the regulatory effect of high-dose TFPH was the most pronounced, which could significantly upregulate PPARα and CPT1A expression, inhibit ACC and FASN expression, and even restore FASN expression to the normal range. This finding is consistent with the significant regulatory effect of TFPH at the metabolomics level, these coordinated shifts in lipid catabolic and anabolic protein levels are correlated with relieved hepatic lipid deposition; the PPARα-mediated fatty acid oxidation pathway may be one associated factor underlying the phenotypic improvement, without confirming direct causal regulation. This mechanism is consistent with the anti-obesity effects and improvement in liver lipid accumulation induced by taxifolin (TFP), and previous studies have shown that taxifolin can reduce cholesterol and triglyceride levels in the livers of mice fed a high-fat diet and improve insulin resistance.

In summary, the results of this study confirmed through nontargeted metabolomics that TFPH can effectively reverse metabolic disorders in model animals, and its regulatory effect focuses mainly on lipid metabolism-related pathways. Western blotting quantification of certain biomarkers further confirmed that TFPH can achieve bidirectional regulation of fatty acid synthesis and metabolic degradation through dose-dependent regulation of the expression of key lipid metabolism proteins such as PPARα, CPT1A, ACC, and FASN, thereby ameliorating lipid metabolism disorders. This study provides comprehensive experimental evidence for the use of TFPH as a potential lipid metabolism regulatory drug and provides novel insights for the treatment of lipid metabolism disorder-related diseases. Future research can further explore the specific molecular mechanisms through which TFPH regulates glycerophospholipid metabolism, cholesterol metabolism, etc., as well as its pharmacokinetic characteristics *in-vivo* to lay a foundation for its clinical application.

In the present study, we detected synchronous alterations in intestinal microbial composition, hepatic metabolomic profiles and lipid regulatory protein expression after TFP intervention. However, all multi-omics and biochemical data are merely observational correlative evidence and cannot confirm definitive causal links between these molecular variations and TFP's liver-protective effects. Complex systemic gut-liver metabolic crosstalk cannot be excluded as confounding factors. Subsequent functional experiments including fecal

microbiota transplantation, germ-free mouse models and single flavonoid monomer intervention assays are necessary to dissect precise causal regulatory pathways. In addition, 16S rRNA sequencing only enables genus-level microbial identification, and metagenomic sequencing will be conducted in follow-up work to achieve species-level functional verification.

Conclusions: This study demonstrated that TFP could significantly ameliorate hepatic functional injury, hepatic steatosis and lipid metabolism disturbance in NASH model mice in a distinct dose-dependent manner, with the high-dose TFP group exhibiting optimal therapeutic efficacy. TFP intervention effectively restored the diversity and structural homeostasis of the intestinal microflora, reversed systemic metabolic disorders, and improved hepatic lipid metabolic balance by downregulating the lipid synthesis-related proteins ACC and FASN and upregulating the key lipid catabolic proteins PPARα and CPT1A. In conclusion, TFP intervention correlates with comprehensive relief of NASH-associated liver injury, concurrent with reshaped intestinal microecology, restored metabolic homeostasis and normalized expression of lipid regulatory proteins. It has great potential as a promising natural hepatoprotective agent for the prevention and treatment of fatty liver diseases in animals.

Author statement: YL, YH, YZ, BC: Investigation, data curation, formal analysis, Writing – original draft, visualization; JS, QZ, WB, HD: Methodology, validation, investigation, resources, software, data curation; XW, RZA, XY: reviewing & editing; XX, WQ, YW: Conceptualization, funding acquisition, project administration, supervision, writing – review & editing.

Ethics and informed consent: All animal procedures were approved by the Institutional Animal Care and Use Committee of Yunnan Agricultural University (Approval No. GXU-2026-172).

Manuscript/data statement: This manuscript/data, or portions thereof, has not been published in another journal, or the work has not been previously published elsewhere.

Funding information: This research was financially supported by the Yunnan Key Laboratory of Veterinary Etiological Biology (Grant No: 202449CE340019) (Fengcai Zou and Xiao Xiao) and the Major Science and Technology Project Plan of Yunnan Provincial Department of Science and Technology (Grant No. 202502AE090054) (Xiao Xiao).

Consent for publication: The authors all agreed to the publication of this paper.

Declaration of competing interest: The authors declare that there are no conflicts of interest.

Data availability: Data will be made available on request.

Acknowledgments: We appreciate the assistance from our distinguished colleagues in the Department of Clinic Veterinary of Yunnan Agricultural University.

REFERENCES

Bak Y, Lee BB, Bharti D, *et al*., 2025. Enzymatic extraction and refinement of narirutin from green yuzu (*Citrus junos*): Its positive regulatory effects on nonalcoholic fatty liver disease and gluconeogenesis. Food Bioscience 74:107896.

Bashir F, Sharif S, Manzoor F, *et al*., 2024. Protective effects of Moringa oleifera leaf extract against silver nanoparticles and arsenic induced hepatotoxicity in rats. Pakistan Veterinary Journal 44:377-383.

Celep NA, Erbas E, Kara H, *et al*., 2004. Silymarin reduces paclitaxel-induced lung damage via downregulating P2X7R expression and inhibiting inflammation and apoptosis in the rats. Pakistan Veterinary Journal 44:169-175.

Cheng S, Liu X, Cheng S, *et al*., 2025. The research mechanism of the gut-liver axis in non-alcoholic fatty liver disease. Pakistan Veterinary Journal 45(4): 1524-1531.

Chen X, Zhang YW, Ren H, *et al*., 2024. RNF5 exacerbates steatotic HCC by enhancing fatty acid oxidation via the improvement of CPT1A stability. Cancer Letters 611:217415.

Chen Y, Jin HQ, Xue YZ, *et al*., 2025. Evaluating the hepatotoxicity of polyvinyl chloride microplastics in ducks: oxidative and fibrotic outcomes. Pakistan Veterinary Journal 45:1733-1743.

Choi SE, Hwang Y, Lee SJ, *et al*., 2022. Mitochondrial protease ClpP supplementation ameliorates diet-induced NASH in mice. Journal of Hepatology 77(3):735-747.

Du YQ, Xu J, Jia JH, *et al*., 2025. Yuzhuo Zhixiao pill can treat nonalcoholic steatohepatitis through modulation of gut microbiota, bile acid and short-chain fatty acid metabolism. Phytomedicine 148: 157348.

Eisinger K, Krautbauer S, Hebel T, *et al*., 2014. Lipidomic analysis of the liver from high-fat diet induced obese mice identifies changes in multiple lipid classes. Experimental and Molecular Pathology 97(1):37-43.

Fang Y, Lin Z, Lv Y, *et al*., 2025. Isolation and preparation of flavonoids from *Glycyrrhiza uralensis* fisch. Using multidimensional chromatography for treating nonalcoholic fatty liver disease. Journal of Molecular Structure 1340: 142516.

Han H, Li J, Tian L, *et al*., 2023. Through regulation of the SIRT1 pathway plant sterol ester of alpha-linolenic acid inhibits pyroptosis thereby attenuating the development of NASH in mice. Journal of Nutritional Biochemistry 119:109408.

He BX, Du XH, Du YL, *et al*., 2018. Association of prepartum hypoleptinemia and postpartum subclinical ketosis in holstein dairy cows. Pakistan Veterinary Journal 38(4):404-408.

Hildebrandt MA, Hoffmann C, Sherrill-Mix SA, *et al*., 2009. High-fat diet determines the composition of the murine gut microbiome independently of obesity. Gastroenterology 137(5):1716-1724.

Hu Z, Zhao J, Liu X, *et al*., 2024. Glycyrrhizin regulates antioxidation through Nrf2 signaling pathway in rat temporomandibular joint osteoarthritis. Journal of Oral Rehabilitation 51(3):611-622.

Imtiaz A, Bin Tahir MT, Zhao M, *et al*., 2025. Non-alcoholic fatty liver disease in poultry: Risk factors, mechanism of development, and emerging strategies. International Journal of Molecular Sciences 26(17):8460.

Jiang J, Yan L, Shi Z, *et al*., 2019. Hepatoprotective and anti-inflammatory effects of total flavonoids of Qu Zhi Ke (peel of Citrus changshan-huyou) on nonalcoholic fatty liver disease in rats via modulation of NF-kappaB and MAPKs. Phytomedicine 64:153082.

Lertpatipanpong P, Janpaijit S, Park EY, *et al*., 2020. Potential anti-diabetic activity of *Pueraria lobata* flower (*Flos Puerariae*) extracts. Molecules 25(17): 3970.

Li N, Zhu C, Fu R, *et al*., 2024. Ginsenoside Rg5 inhibits lipid accumulation and hepatocyte apoptosis via the Notch1 signaling pathway in NASH mice. Phytomedicine 124:155287.

Li S, Ma S, Wang P, *et al*., 2025. *Flos puerariae* derived exosomes-like nanoparticles ameliorate alcoholic liver disease by targeting IL-11-related signaling pathways and reactive oxygen species. Chemical Engineering Journal 512: 161896.

Li Y, Zhang L, Jiao J, *et al*., 2023. Hepatocyte CD36 protects mice from NASH diet-induced liver injury and fibrosis by blocking N1ICD production. Biochimica et Biophysica Acta-Molecular Basis of Disease 1869(7):166800.

Liu K, Mehmood K, Li Y, *et al*., 2025. Baicalin is accompanied by correlative changes in CDH11/Wnt/β-catenin Pathway: A novel therapeutic strategy against tibial dyschondroplasia in broiler chickens. Pakistan Veterinary Journal 45:1146-1156.

Lombardo E, van Roomen CP, van Puijvelde GH, *et al*., 2012. Correction of liver steatosis by a hydrophobic iminosugar modulating glycosphingolipids metabolism. PLoS One 7(10):e38520.

Makatjane KA, Zhou H, 2026. Research progress on plant flavonoids as a strategy against oxidative stress in broilers: mechanistic insights and the potential of Silphium perfoliatum L.: review. Animal Diseases 6:8.

Niu T, Wang J, Xun L, *et al*., 2024. Deciphering the impact and mechanism of total flavonoids from Cortex Juglandis Mandshuricae on alcoholic fatty liver employing LC–MS/MS, network pharmacology analysis and *in-vitro* validation. Journal of Chromatography B 1248:124334.

Panyod S, Wu WK, Hu MY, *et al*., 2024. Healthy diet intervention reverses the progression of NASH through gut microbiota modulation. Microbiology Spectrum 12(1): e01868-23.

Qureshi IA, Khan SA, Chaudhry ZI, *et al*., 2004. Effects of high dietary fat on serum cholesterol and fatty liver syndrome in broilers. Pakistan Veterinary Journal 24(3):153-154.

Shaukat A, Rajput SA, Hanif S, *et al*., 2025. Morin inhibits inflammation, oxidative stress and ferroptosis in lipopolysaccharide-induced endometritis. Pakistan Veterinary Journal 45:799-806.

Shu YY, Hu LL, Ye J, *et al*., 2024. Rifaximin alleviates MCD diet-induced NASH in mice by restoring the gut microbiota and intestinal barrier. Life Sciences 357:123095.

Su H, Wang WJ, Zheng GD, *et al*., 2022. The anti-obesity and gut microbiota modulating effects of taxifolin in C57BL/6J mice fed with a high-fat diet. Journal of the Science of Food and Agriculture 102(4):1598-1608.

Tu W, Zhang Y, Jiang K, *et al*., 2023. Osteocalcin and its potential functions for preventing fatty liver hemorrhagic syndrome in poultry. Animals 13(8):1380.

Vemula S, Mylaram J, Yadala R, *et al*., 2025. Protective effects of naringenin on 5-fluorouracil induced pulmonary toxicity via modulation of NF-κB and Nrf2 pathway. Pakistan Veterinary Journal 44:63-70.

Wei S, Wang L, Evans PC, *et al*., 2024. NAFLD and NASH: etiology, targets and emerging therapies. Drug Discovery Today 29(3):103910.

Wu L, Yan M, Jiang J, *et al*., 2017. Pure total flavonoids from citrus improve nonalcoholic fatty liver disease by regulating TLR/CCL signaling pathway: A preliminary high-throughput 'omics' study. Biomedicine & Pharmacotherapy 93:316-326.

Xiong Y, Yang Y, Yang J, *et al*., 2010. Tectoridin, an isoflavone glycoside from the flower of Pueraria lobata, prevents acute ethanol-induced liver steatosis in mice. Toxicology 276(1):64-72.

Xiong Y, Zhu C, Chen Y, *et al*., 2026. Ginsenoside CK regulates nonalcoholic fatty liver disease by regulating liver fat metabolism and gut microbiota. International Immunopharmacology 174:116338.

Xu J, Sui J, Luo Y, *et al*.,2025. The protective and therapeutic effects of herbal medicines on hepatic disorders in animals. Pakistan Veterinary Journal 45(4): 1491-1502.

Yan LS, Kang JY, Gu CY, *et al*., 2025. *Schisandra chinensis* lignans ameliorate hepatic inflammation and steatosis in methionine choline-deficient diet-fed mice by modulating the gut-liver axis. Journal of Ethnopharmacology 348:119801.

Yan T, Luo Y, Yan N, *et al*., 2023. Intestinal peroxisome proliferator-activated receptor alpha-fatty acid-binding protein 1 axis modulates nonalcoholic steatohepatitis. Hepatology 77(1):239-255.

Zhan Y, Li Q, Li T, *et al*., 2024. *Lactobacillus plantarum* P9 ameliorates dysfunctional immune and metabolic homeostasis along the gut-liver axis in a nonalcoholic fatty liver disease with low-grade colitis mouse model. Food Bioscience 61:104613.

Zhang C, Zhang M, Wang S, *et al*., 2010. Interactions between gut microbiota, host genetics and diet relevant to development of metabolic syndromes in mice. ISME Journal 4(2):232-241.

Zhao J, Jin J, Li Y, *et al*., 2025. Yinchen-Gancao decoction ameliorated NASH in mice by reducing hepatic lipid accumulation, inhibiting hepatic inflammatory and endoplasmic reticulum stress. Journal of Ethnopharmacology 341:119318.

Zhu H, Xing Y, Akan OD, *et al*., 2023. Ultrafine comminution-assisted ultrasonic-microwave synergistic extraction of *Pueraria mirifica* (Kudzu flower and root) flavonoids. Heliyon 9(11):e21137.

Zhu L, Baker RD and Baker SS, 2015. Gut microbiome and nonalcoholic fatty liver diseases. Pediatric Research 77(1-2):245-251.